Review article

Jiafang Li* and Zhiguang Liu

Focused-ion-beam-based nano-kirigami: from art to photonics

Abstract: Kirigami, i.e. the cutting and folding of flat objects to create versatile shapes, is one of the most traditional Chinese arts that has been widely used in window decorations, gift cards, festivals, and various ceremonies, and has recently found intriguing applications in modern sciences and technologies. In this article, we review the newly developed focused-ion-beam-based nanoscale kirigami, named nano-kirigami, as a powerful three-dimensional (3D) nanofabrication technique. By utilizing the topography-guided stress equilibrium induced by ion-beam irradiation on a free-standing gold nanofilm, versatile 3D shape transformations such as upward buckling, downward bending, complex rotation, and twisting of nanostructures are precisely achieved. It is shown that the generated 3D nanostructures possess exceptional geometries and promising photonic functionalities, including strongly interacting multiple Fano resonances, giant optical chirality, clear photonic spin Hall effects, and diffractive phase/polarization effects. The studies of such structures can build up novel platforms for versatile manufacturing techniques and be helpful to establish new areas in plasmonics, nanophotonics, optomechanics, MEMS/NEMS, etc., with the generation of exotic but functional nanostructures.

Keywords: nano-kirigami; three-dimensional nanofabrication; focused ion beam; optical chirality; metasurfaces.

*Corresponding author: Jiafang Li, Institute of Physics, Beijing National Laboratory for Condensed Matter Physics, Chinese Academy of Sciences, Beijing 100190, China,
e-mail: jiafangli@aphy.iphy.ac.cn. http://orcid.org/0000-0002-9658-8261
Zhiguang Liu: Institute of Physics, Beijing National Laboratory for Condensed Matter Physics, Chinese Academy of Sciences, Beijing 100190, China; and University of Chinese Academy of Sciences, Beijing, 100049, China

1 Introduction

Kirigami, i.e. the cutting and folding of flat objects to create versatile shapes, is one of the most traditional Chinese arts (named "jianzhi") and plays important roles in people's daily lives [1], such as the paper-cuts used frequently in window decorations, gift cards, festivals, and various ceremonies. The symbolic role of kirigami and origami (origami does not involve the cutting process), as recorded in the famous Chinese book of "Records of the Grand Historian", existed much before the invention of paper (around 105 A.D. in China). For example, around 1055–1021 B.C., King Cheng of the Zhou Dynasty patterned one leaf of a Chinese parasol tree and treated it as a pledge to award his brother a territory [2]. The earliest example of paper-based kirigami, named "Flowery Horses" [2], was found in a relic of the Chinese Northern Dynasties (386–581 A.D.). During the 6th century, paper was introduced into Korea and then into Japan [3], where the kirigami and origami emerged as special symbols in religious rituals and important ceremonies. Different from ancient Chinese who treated kirigami and origami as phenomenological skills, Japanese pioneers have recorded and analyzed the detailed methods of these ancient arts since the 17th century, benefiting from which the knowledge of kirigami and origami has been well accumulated and communicated in Japan and other regions of the world. In the West, kirigami and origami might have been developed independently as ceremonial symbols in the 15th century and later on became popular as gifts, occupations, or art forms among the social elites [3]. It was in 1962 that the English word "kirigami" was coined by Florence Temko from the Japanese words *kiri* (meaning "cut") and *kami* (meaning "paper") [4].

Beyond their significances in arts and architectures, modern kirigami and origami have aroused tremendous interests in the frontiers of both fundamental sciences and practical applications, such as deployable designs for satellite solar arrays [5], micro-/nano-electromechanical systems (MEMS/NEMS) [6], energy storage systems [7], biomedical devices [8], micro-/nanoscale mechanical and photonic materials [9–13], etc. Among them, the

area of three-dimensional (3D) micro-/nanofabrication has shown the great potentials of kirigami [14–17] because of its rich shape transformations from 2D precursors to 3D architectures without the need of precise 3D translation as in direct lithography [18, 19] or accurate alignment during indirect multilayer stacking [20]. However, one major issue of kirigami is that, when it comes to the nanoscale (e.g. nano-kirigami), it is extremely difficult to find a direct and sophisticated enough "nano-hand" and a "nano-cutter" to accomplish the nano-kirigami process, like the way employed by macroscopic kirigami. Alternatively, indirect procedures with multiple materials and multiple steps, as in most mesoscopic kirigami and origami methods, utilized the differential strains between neighboring objects to achieve spontaneous curving or folding [15, 21–23], which can be triggered by stimuli like temperature changes, volume variations, capillary forces, residual removal, etc. However, these multistep procedures have to be carefully predesigned and sequentially performed, making it challenging to instantly add/ remove desirable components onsite. Meanwhile, most of the studies on kirigami and origami have been primarily aimed at shape transformation or mechanical characterization because of their relatively large scales. The versatile 3D geometries brought by nano-kirigami, intuitively desirable for exceptional optical, electric, magnetic, thermal, and nanomechanical functionalities, have not yet been fully explored.

In comparison, a focused ion beam (FIB) possesses fabrication resolution down to several nanometers and has become popular as a direct and powerful machining tool since its successful applications in the semiconductor industry from the 1980s [24]. Besides the FIB-induced deposition method [25], FIB has been mostly utilized as a lithography tool, which can be treated as an accurate "nano-cutter" for kirigami. Interestingly, recent studies have shown that FIB irradiation on nanoscale freestanding thin films can result in the folding and assembly of nanostructures [26–34], implying its potential to be a "nano-hand". For example, in 2006, Xia et al. [26] reported the fabrication of 3D helix and cubic frames with FIB-induced stress, which was soon adopted by Arora et al. in 2007 [27, 28] and other groups in later researches [29–31, 35, 36]. In 2015, the first photonic application of this method was demonstrated by Cui et al. through folding a vertical split-ring resonator (SRR) array in the optical region [30], which generated enormous interest in photonics such as extraordinary Fano resonances [31, 37], toroidal mode generation [34], reversible mid-infrared switching [33], and chiral optical antennas [38]. However, all these methods, as well as their applications, have

not been considered as "nano-kirigami" because of their sequential procedures inducing tree-type shape transformation. It was only very recently that nano-kirigami was realized based on topography-guided 3D nanofabrication of complex and functional photonic nanostructures with global FIB irradiation [39]. The involved onsite buckling, rotation, and twisting of nanostructures during the continuous 3D shape transformation clearly reflected the intrinsic features of macroscopic kirigami, and the reliable sub-50-nm resolution unambiguously entered the realm of nano-kirigami.

To uncover the significances and explore the potentials brought by such a new type of 3D nanofabrication method, in this article we review the previous studies on FIB-based sequential folding/bending as "tree-type nano-kirigami" and the recent topography-guided shape transformation with FIB as "close-loop nano-kirigami". Versatile, unprecedented 3D nanogeometries will be introduced with both types of nano-kirigami methods. More importantly, photonic functionalities of the generated structures, including strongly interacting multiple Fano resonances, giant optical chirality, clear photonic spin Hall effects (SHEs), and diffractive phase/polarization effects, will be introduced. The studies could build up novel platforms for versatile manufacturing techniques such as intelligent 3D nanofabrication and can be helpful in establishing new areas in plasmonics, nanophotonics, optomechanics, MEMS/NEMS, etc., with the generation of exotic while functional nanostructures.

2 Folding/bending mechanism with FIB

FIB-based nano-kirigami is mainly based on a gallium-ion dual-beam FIB/SEM system (FEI Helios 600i) under a high acceleration voltage of 30 kV, whose fabrication principle can be extended to other platforms. Operated on a suspended gold nanofilm (with ~80 nm thickness) [39], the nano-kirigami process includes a high-dose FIB milling and a subsequent low-dose irradiation of the effective sample area, which can be programmed into one step. Specifically, when the gold nanofilm is irradiated by the high-energy gallium ions, four main processes occur [28]: (i) some gold atoms are sputtered away from the surface, thereby creating vacancies; (ii) some gallium ions are implanted into the gold film; (iii) some gold atoms within the film are dislocated as a result of the collisions; and (iv) some gold and gallium atoms re-deposit on the film surface. The range of vacancies and ion implantation

can be well predicted by the SRIM software, which is based on a Monte Carlo simulation method, as shown in Figure 1A–C. These modifications in the distribution of atoms will introduce local stress, strain, or deformation of the thin film. Actually, the undesirable stress, surface damage, and implantation induced by FIB have long been considered as drawbacks for applications such as transmission electron microscopy (TEM) sample preparation and diagnosis.

Here, the nano-kirigami method is introduced by making good use of this "undesirable" residual stress [39]. As illustrated in Figure 1A, when the gold thin film is exposed to ion irradiation, the resulting vacancies cause the grain to coalesce and induce tensile stress close to the film surface. Meanwhile, the implanted gallium ions get lodged into the atomic lattice and introduce a compressive stress. These two types of stress occur simultaneously within ~20 nm of the gold film (Figure 1B and C) and are dominant during ion-beam irradiation. Their combination

determines the overall stress within the ion-beam-affected top layer, which deforms the less affected bottom layer of gold. Our tests show that the tensile stress is dominant when FIB with an acceleration voltage of 30 kV is applied to a 80-nm-thick gold film [39]. Therefore, the free-standing gold film in our case can be simplified into a bilayer model, i.e. the top amorphous layer with tensile stress and the bottom layer with deformation stress. In such a simplified model, when one end of the suspended structure is fixed, the top tensile stress will cause the suspended structure to bend upward, as illustrated in Figure 1D. Alternatively, when both boundaries of the cantilever are fixed, the suspended structures could bend downward under the topography-guided stress equilibrium [39]. Meanwhile, the scanning strategy of the ion-beam irradiation influences the structural deformations dramatically. As shown in Figure 1E, the local irradiation under line-scanning along a specific line (defined as the hinge line) induces zero curvature except at the abruptly changed
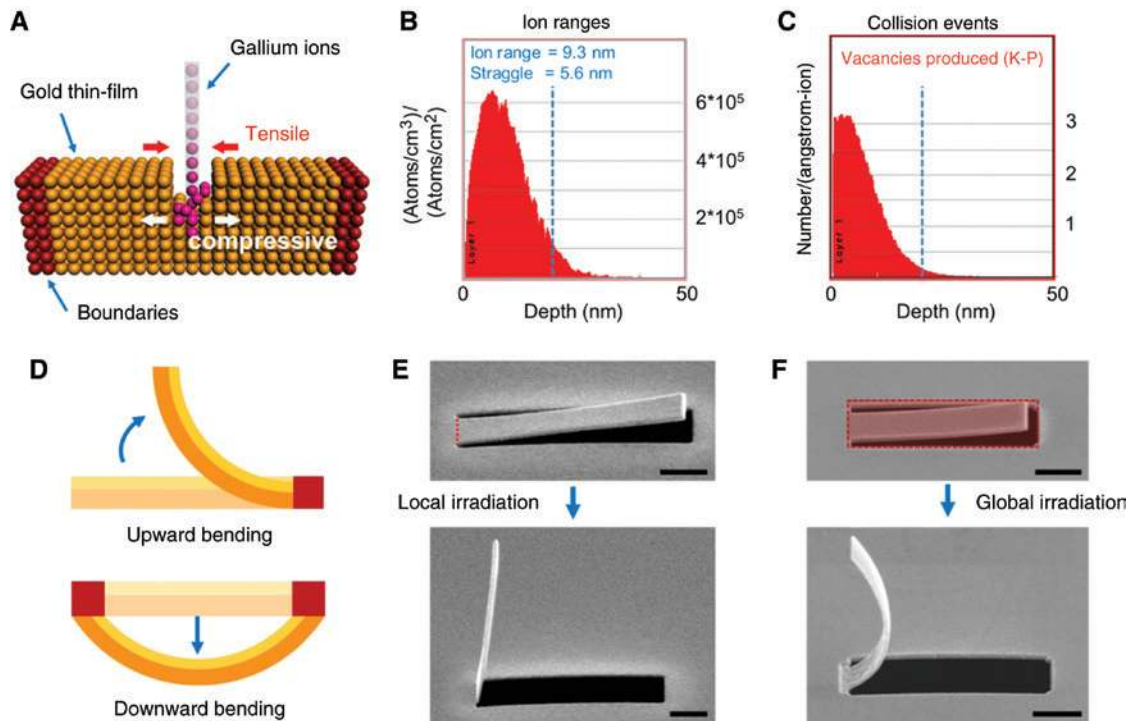

Figure 1: Mechanism of FIB-based nano-kirigami.
(A) Schematic illustration of residual stress distribution within a free-standing gold nanofilm under FIB irradiation [39]. (B, C) Simulated distributions of (B) gallium ion concentration and (C) vacancy density versus the depth of the nanofilm using SRIM software under FIB irradiation with acceleration voltage of 30 kV [39]. (D) Schematic of two typical structural deformations when only one or two ends (indicated by the red squares) of the suspended structures are fixed, which are determined by the stress equilibrium [39]. When one end is fixed, the cantilever will bend upward, which releases the tensile stress. When both ends of the cantilever are fixed, the bending of the film can no longer release the tensile stress due to the increased length. In such a case, the compressive stress and the dislocation (diffusion) of the gold atoms take important effects, which could cause the cantilever to bend downward under certain topography-guided stress equilibrium. (E, F) Side-view SEM images of (E) rigid folding and (F) gradual bending of suspended cantilevers under local and global FIB irradiations over the red areas, respectively [40]. Scale bars: 1 μm. (The thickness of the gold nanofilm is 80 nm in this article, if not mentioned otherwise).
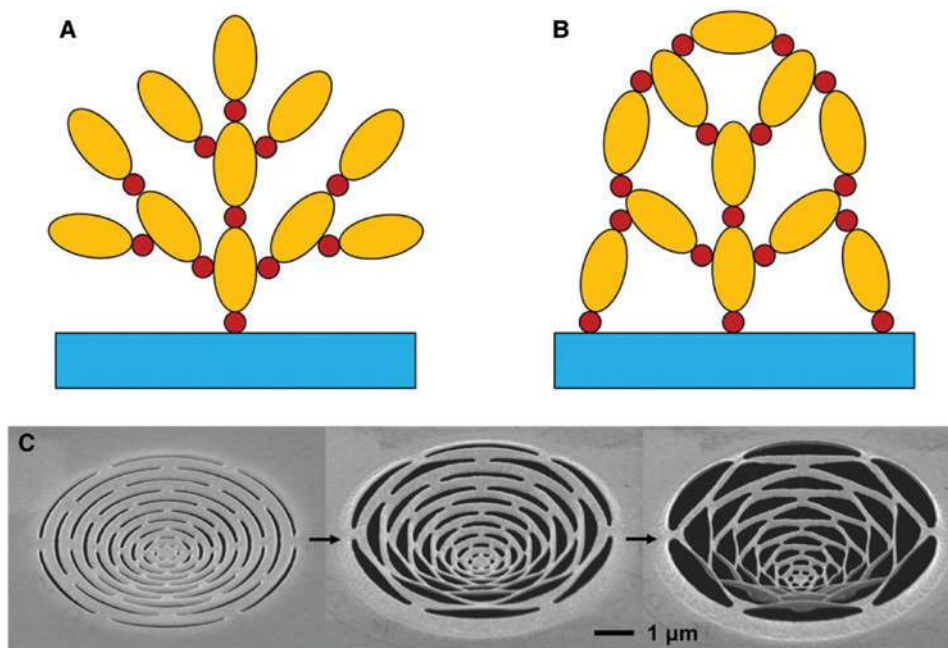
Figure 2: Schematic of the topological classifications of multibody systems that can be used to differentiate the types of nano-kirigami methods [41, 42].
(A) Tree-type system. The relative motions within each neighboring (represented by the orange ellipses) object are independent. (B) Close-loop system. The relative motions of subunits within the loop interact with each other. The hinges are represented by the red circles. (C) SEM images of a typical example of close-loop nano-kirigami [39]. A 2D concentric-arc structure can bend downward gradually under increased global ion-beam irradiation, which is caused by the topography-guided stress equilibrium.
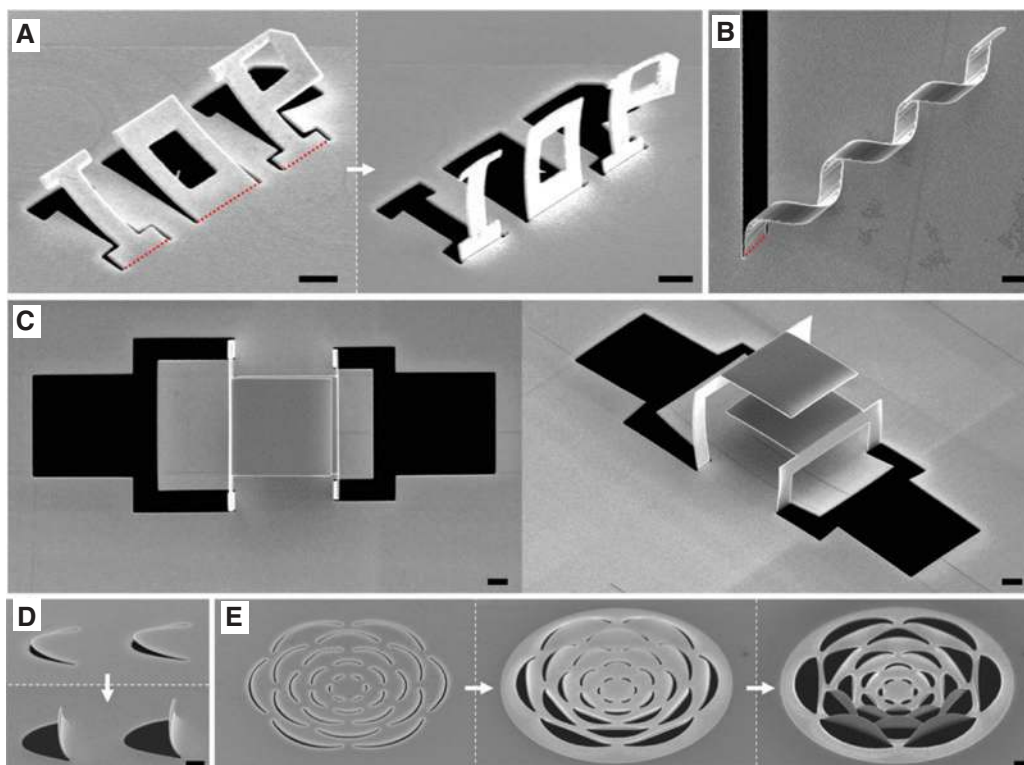

Figure 3: FIB-based tree-type folding/bending.
(A–C) Local FIB-irradiation-induced folding of (A) "IOP" letters, (B) a horizontal spiral, and (C) a triple-layer structure. (D, E) Global FIB-irradiation-induced bending of (D) tongue-like and (E) flower-like structures [39]. Scale bars: 1 μm.

regions, causing rigid folding [40]. In comparison, global irradiation under frame-scanning causes the gradual bending of the micro-stripe, introducing continuous curvatures [40], as shown in Figure 1F. Such topography-guided and irradiation-dependent folding/bending of the suspended nanostructures constitutes the basic principle of nano-kirigami in this study.

3 Tree-type folding/bending with FIB

Taking the FIB-induced stress as a stimulus, FIB-based nano-kirigami can be sorted into two types from the viewpoint of topological classifications in multibody dynamics [41, 42]. One is the tree-type folding/bending with FIB, in which the relative motions within each neighboring object are independent (Figure 2A) [42], i.e. the shape transformation among different branches with this method is relatively isolated (the other one is the more advanced close-loop nano-kirigami which will be introduced in the next section). As shown in Figure 3, in the tree-type nano-kirigami method, 3D structures with various geometries can be formed by locally folding the nanostructures

along well-designed hinge lines through sequential FIB line-scanning (Figure 3A–C), or simultaneously bending the isolated subunits of 2D patterns under global FIB frame-scanning (Figure 3D–E). Because of its streamlined feature, such tree-type method is well suited for fabricating arrays of upright nanostructures with regular geometries, as shown in Figure 4. As a matter of fact, such tree-type folding/bending with FIB has been investigated in many pioneering studies since 2006 [26–31, 33–36, 38], which, however, have not yet been recognized as "nano-kirigami" approaches because of their simple shape transformation compared to the classical kirigami methods.

4 Close-loop nano-kirigami with FIB

The more advanced and complex 3D shape transformation, in analogy with the macroscopic paper-cuts, is the FIB-based close-loop nano-kirigami [39], in which the relative motions of the subunits within the loop become interactive, i.e. the motion of one object influences the relative motions of the others, as illustrated in Figure 2B and C. Actually, the interrelated shape transformation of neighboring subunits represents one of the most intrinsic
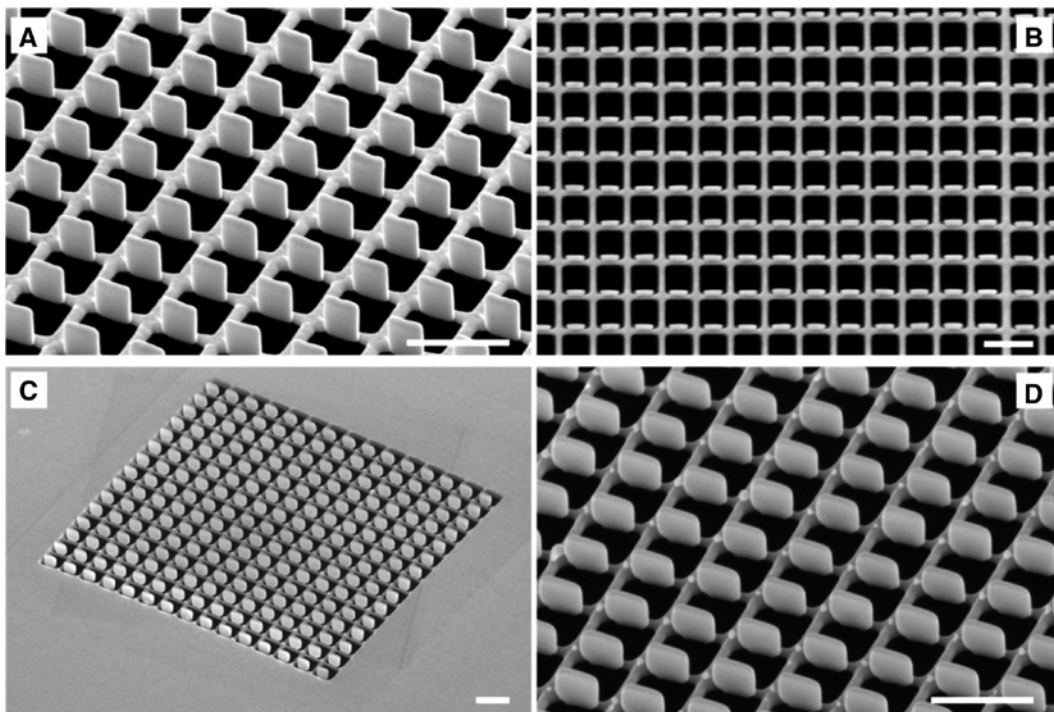

Figure 4: Vertical plate arrays fabricated by tree-type nano-kirigami.
(A, B) Side-view and top-view SEM images of vertical plates standing along one edge of the planar metallic hole arrays. (C, D) Side-view SEM images of the same design as in (A, B) but fabricated in an 80-nm gold film deposited on a commercial SiN film window (30 nm thick). Lattice constant: 700 nm. Scale bars: 1 μm.

natures of kirigami/origami and provides an extra freedom toward 4D manufacturing [14], which is highly desirable but has not aroused sufficient interest in the nanorealm. To this end, here we show that close-loop folding/bending with FIB fits the concept of "close-loop nano-kirigami" very well, in comparison with which we summarize the previous studies on FIB-based sequential folding and bending as "tree-type nano-kirigami".

Figure 5 shows the close-loop folding of complex 3D structures under local FIB irradiation, where the multiple foldings around the hinge lines are interlinked. Specifically, some parts of the structures can be folded by the interaction with other branches without direct FIB irradiation. In these cases, the positions of the hinge lines have to be carefully designed and "simultaneously" irradiated

by FIB. For example, in Figure 5B, both ends of the plate, marked by the red double-headed arrows, change their positions dynamically during the rising of the structure, making it impossible for specific FIB irradiation to track the ends of this plate. To solve this issue, two connecting hinge lines were predesigned at the ends of the plate and "passive" deformation was induced by the movement of neighboring objects, reflecting the intrinsic features of the close-loop system. This strategy can be readily applied for multiple pop-up plates, as shown in Figure 5C. Similarly, as in Figure 5D, the star-like structure can only be folded upward under parallel FIB scanning along the multiple dashed lines.

Beyond the local irradiation, the global FIB illumination can induce more advanced close-loop nano-kirigami.
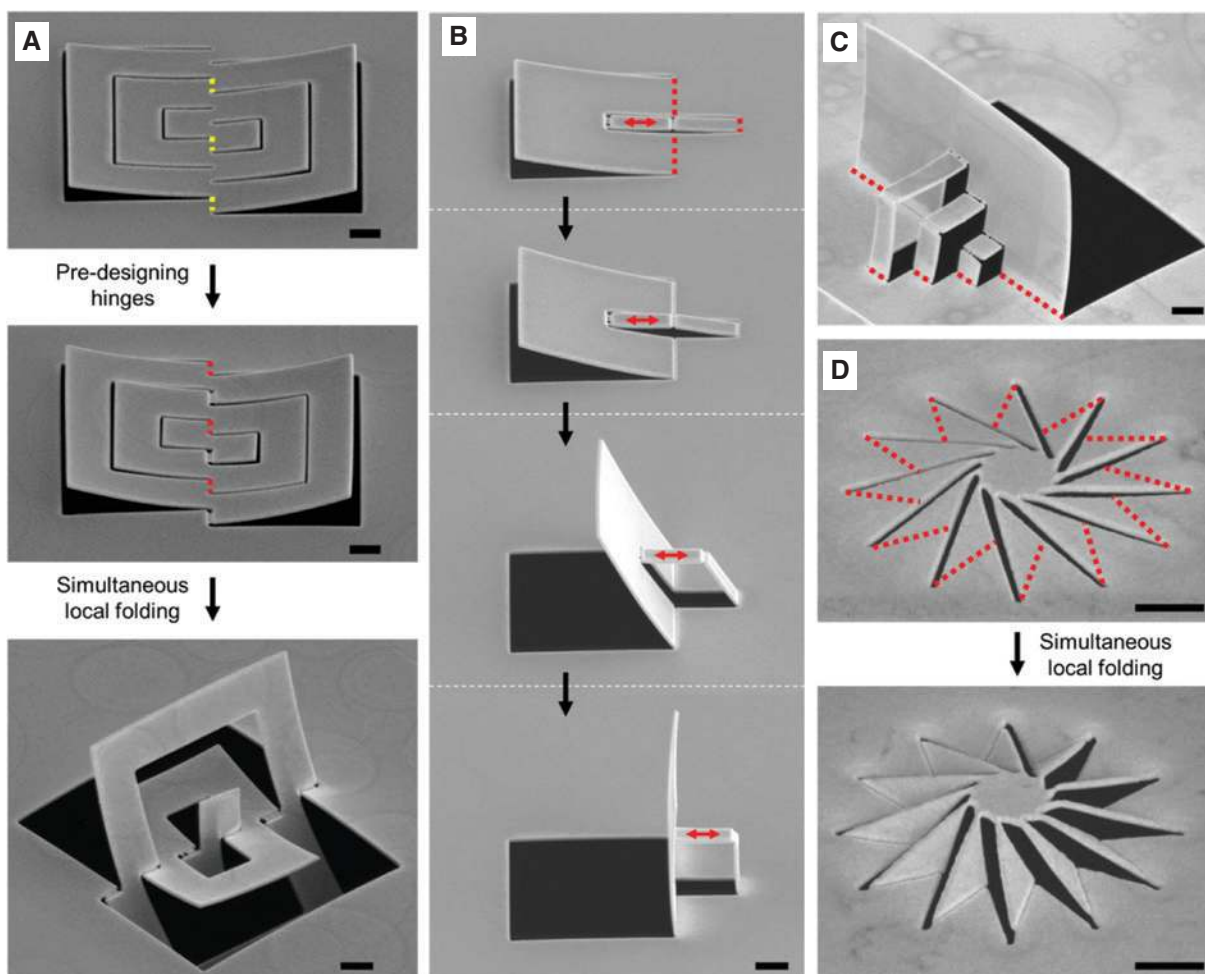

Figure 5: Local FIB-irradiation-enabled close-loop nano-kirigami.
(A) Fabrication of a nested-frame structure by predesigning hinge lines along the yellow dashed lines and then parallel scanning along the red dashed lines with local FIB irradiation. (B) Fabrication of a pop-up plate by parallel FIB scanning along the red dashed lines [40]. The rectangular plate, denoted by the double-headed arrow, is popped up by the forces delivered from the neighboring subunits during their upward foldings. (C) Multiple pop-up plates induced by parallel FIB irradiation along the red dashed lines. (D) Fabrication of a star-like structure under parallel FIB irradiation along the red dashed lines. Scale bars: 1 μm.
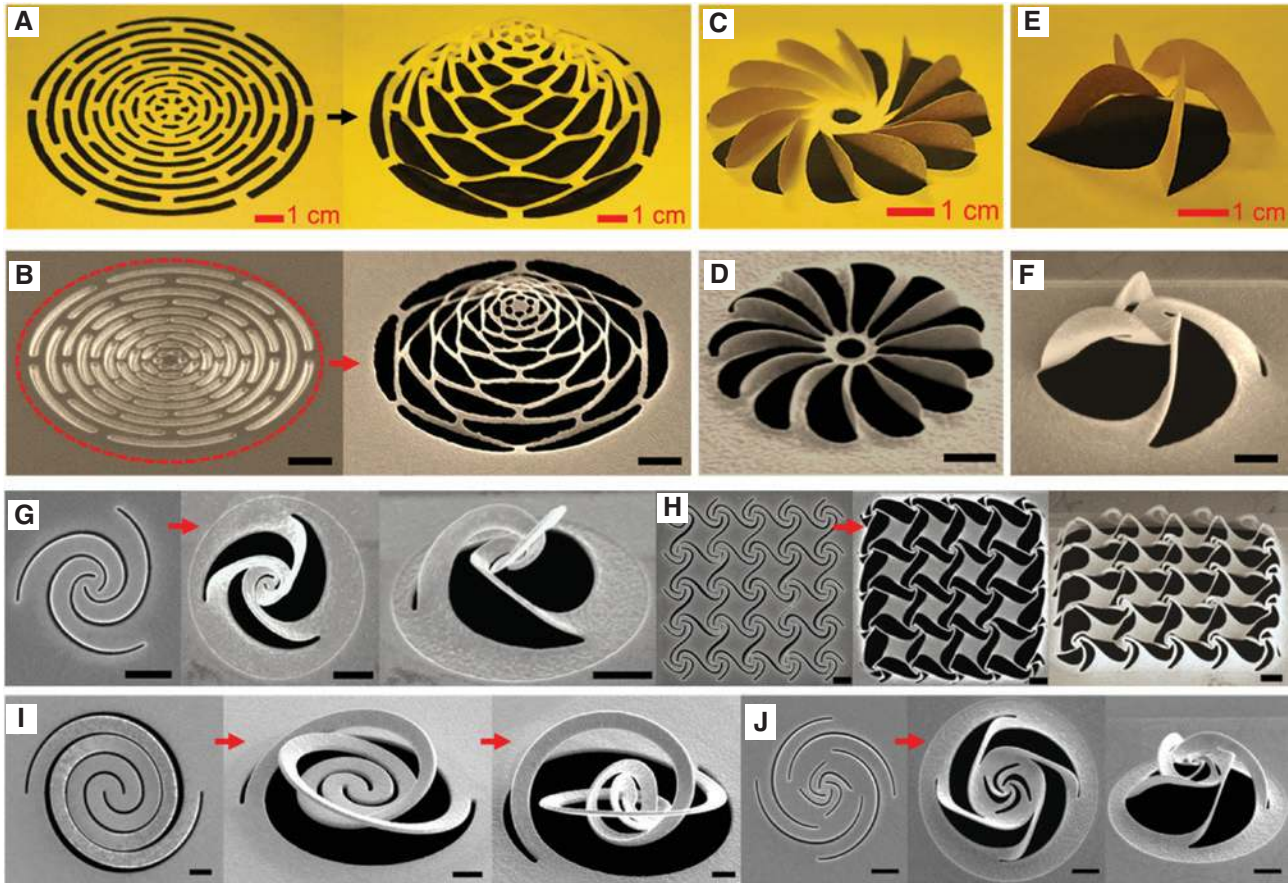
Figure 6: Macro-kirigami by hand and close-loop nano-kirigami by global FIB irradiation [39].
(A, C, E) Camera images of the macroscopic paper kirigami of (A) an expandable dome, (C) a 12-blade propeller, and (E) a four-arm pinwheel.
(B, D, F) Corresponding microscopic structures reproduced by close-loop nano-kirigami with global FIB irradiation. (G–J) Top-view and side-view SEM images of typical structures before and after global FIB irradiation: (G) a twisted triple Fibonacci spiral; (H) window-decoration-type nanobarriers; (I) a deformable spiral; (J) a combined spiral structure. Scale bars: 1 μm.

As illustrated in Figure 6A and B, the macroscopic paper-cut of an expandable micro-dome is well reproduced in the nanoscale by the close-loop nano-kirigami with global FIB irradiation, which is impossible with local FIB irradiation. Such advantages could be applied for the generation of exotic 3D structures with unprecedented geometries, such as a 12-blade propeller (Figure 6C, D), a four-arm pinwheel (Figure 6E, F), twisted triple Fibonacci spirals (Figure 6G), window-decoration-type nanobarriers (Figure 6H), a deformable spiral (Figure 6I), and a combined spiral heterostructure (Figure 6J).

5 Photonic applications of FIB-based nano-kirigami

Although FIB-based tree-type folding/bending aroused some interest in the past decade, most of the studies were focused their potentials on shape transformation or mechanical applications. It was in 2015 that Cui et al. [30] first explored the photonic properties of a "nanograter" structure consisting of vertical SRRs (Figure 7A), which exhibited unusual and ultrasensitive Fano resonances in the near-infrared (NIR) wavelength region. Further studies showed that this tree-type folding was highly desirable to generate vertical 3D nanostructures that possessed a unique 3D plasmonic conductive coupling mechanism [31, 37]. In this mechanism, the planar metallic holes generate "bright" plasmonic resonances that drive the "dark" plasmonic modes along the edges of vertical structures. As a result, the replacement of vertical SRRs by using vertical plates can introduce similar Fano resonances (Figure 7B–G). By taking advantage of the 3D conductive couplings, more vertical elements can be integrated onto the planar arrays. For example, by assembling vertical double plates or four SRR structures, fivefold Fano resonances [43] or high-quality toroidal modes [34] have
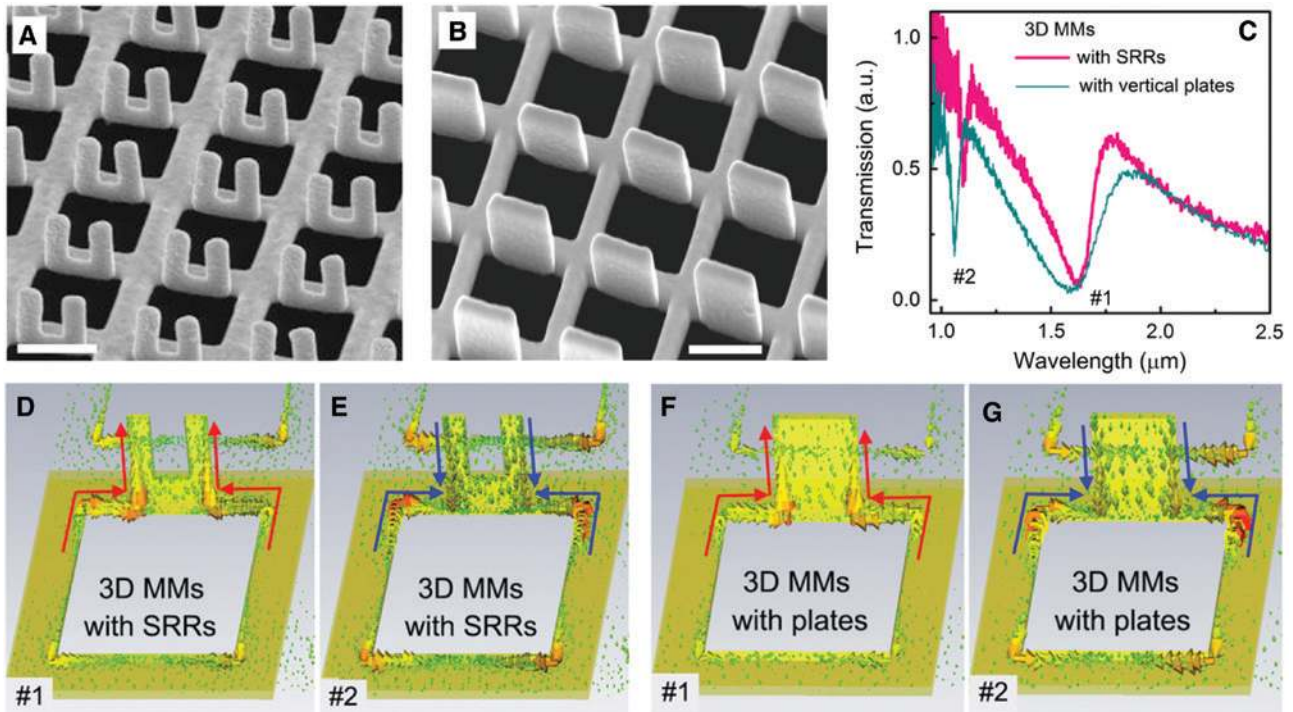
Figure 7: 3D conductive-coupling-induced significant Fano resonances [31].
(A, B) SEM images of 3D metamaterials (MMs) with (A) vertical SRRs and (B) vertical plates standing along metallic hole arrays, which were folded upward by local FIB irradiation. Scale bars: 500 nm. (C) Measured transmission spectra of the structures in (A, B) under *y*-polarized light excitation, which have similar profiles with two resonance modes #1 and #2, respectively. (D–G) Simulated current distributions of the two structures with vertical (D, E) SRRs and (F, G) plates, respectively, at the wavelength of modes #1 and #2.

been generated by using FIB-based tree-type folding. More importantly, the generation of new geometries facilitates the exploration of new physics. For instance, by employing a symmetry-broken SRR-based configuration, double Rabi splittings in triple Fano resonances were clearly observed [37], which agreed excellently with rigorous numerical simulations and theoretical modeling, as shown in Figure 8. It should be mentioned that such an important system related with the interaction among multiple discrete states and one continuum was theoretically mentioned by Fano in 1961 [44] but had not been realized earlier in atomic or optical systems.

Compared with the tree-type folding method, the close-loop nano-kirigami with FIB is able to produce more advanced nanogeometries. For example, the out-of-plane twisting by close-loop nano-kirigami can help facilitate unique photonic properties such as 3D optical chirality [39, 40]. This is unique compared with the 2D structures in that intrinsic chirality [45–48] – the geometric property of a structure lacking any mirror symmetry plane – exists only in three dimensions. Therefore, by utilizing the exotic geometries, a 3D pinwheel structure was designed based on the evolution from vertical helices and horizontal cross-linked helices [39], as illustrated in Figure 9A.

Because of the twisted loops in all directions, the electric field (E_x) of the incident light could induce both electric ($p_{x,L}$) and magnetic ($m_{x,L}$) moments in the parallel direction (i.e. $p_{x,L}//m_{x,L}//x$) for the left-handed (LH) pinwheel, as illustrated in Figure 9B. Since optical chirality is dependent on the strength of $\boldsymbol{p} \cdot \boldsymbol{m}$, the parallel electric and magnetic moments can interact strongly to induce pronounced optical chirality. Meanwhile, the direction of the induced electric and magnetic moments is highly dependent on the LH or right-handed (RH) twisting of the four arms (Figure 9C), resulting in LH or RH chiral responses [39]. For experimental demonstrations, Figure 9E shows the SEM images of 3D pinwheels after nano-kirigami of the 2D planar array (Figure 9D), where the 3D twisted arms are clearly identified. Because of the twisted loops in all directions [45], parallel electric and magnetic moments are introduced and interact with each other, which fundamentally induce giant optical chirality [39]. For example, a giant polarization rotation versus wavelength is observed, as plotted in Figure 9F and G, in which the polarization rotation angle reaches ~90° at 1.70 μm. Considering the overall structural thickness of ~430 nm (including the bottom layer), such circular birefringence is equivalent to ~210,000°/mm, which is giant-sized compared to the
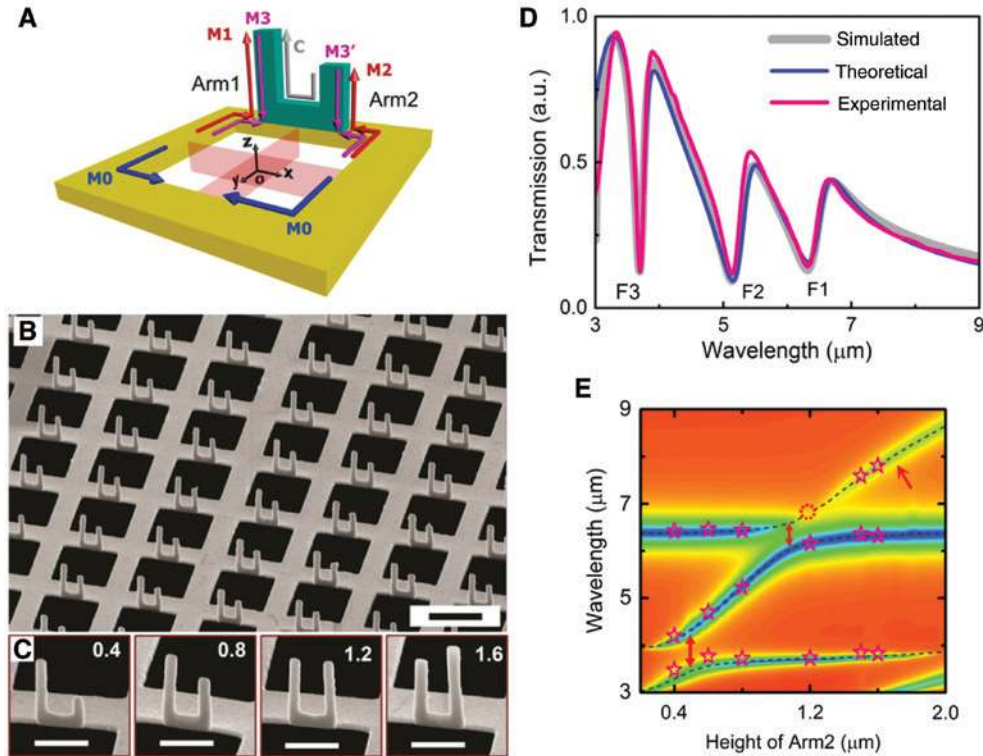
Figure 8: Strong interactions among triple Fano resonances [37].
(A) Schematic of the unit cell of a 3D nanostructure, which consists of a vertical asymmetric SRR (aSRR) standing along one edge of a metallic hole. The arrows in different colors indicate different types of current oscillations existing within the unit cell, which correspond to one bright mode (M0) and three dark modes (M1, M2, and M3/M3'). The mode M0 interacts with modes M1, M2, and M3, respectively, which results in the triple Fano resonances F1, F2, and F3 in (D). (B, C) SEM images of aSRRs with different arm lengths standing along one edge of metallic holes. (D) Simulated, theoretical, and experimental transmission spectra of the array in (B), which show excellent agreement. (E) Color map of the simulated absorption spectra of the aSRRs versus the height of Arm2. The dashed curves show the calculated wavelengths of Fano resonances, and the red stars correspond to the experimental measurements. Scale bars: 1 μm.

statistics of chiral metamaterials and planar structures in the literature [49]. These experimental results agree well with the calculations and unambiguously demonstrate the significance brought by the close-loop nano-kirigami.

The optical chirality of the 3D pinwheel could be further employed to explore versatile functionalities such as polarization conversion and phase engineering in metasurfaces [40, 50–54]. As plotted in Figure 10A, under x-polarized excitation, the cross-polarized (y-polarized) transmission of the LH and RH 3D pinwheels has a phase difference of π over a broad band (1.45–3.0 μm). Therefore, by arranging the LH and RH windmills alternatively with a period L along the x-axis, as shown in Figure 10B, a binary diffractive grating for the cross-polarized light is formed. According to general diffraction theory, and under x-polarized excitation, the cross-polarized beams (y-polarized light) will be diffracted by an angle α (Figure 10C), which satisfies $L \sin \alpha = (m - 1/2)\lambda$, $m = 0, \pm 1, \pm 2, \ldots$. These characteristics are well verified by the recorded images

in Figure 10D. For example, at the wavelength of 1.68 μm where the cross-polarized transmission is close to the maximum, the center spot from the original beam is hardly seen because most of the light is converted into the diffracted components with y-polarization. In comparison, only the center spot is observed at wavelength 1.2 μm since the cross-polarized transmission is nearly zero at this wavelength. At an intermediate wavelength of 1.6 μm, both the center spot and diffracted spots are clearly seen.

More interestingly, it is found that diffractive polarization conversion not only works with linearly polarized incidence but is also applicable for the circularly polarized waves (Figure 10E), i.e. the phase gradient in Figure 10B is also applicable for circular polarization conversion [40]. Therefore, in Figure 10E the spots shift along the x-axis as a result of the diffraction of the cross-polarized right circularly polarized (RCP) and left circularly polarized (LCP) beams. Importantly, a close look at Figure 10E shows that the image spots move slightly along the y-direction and
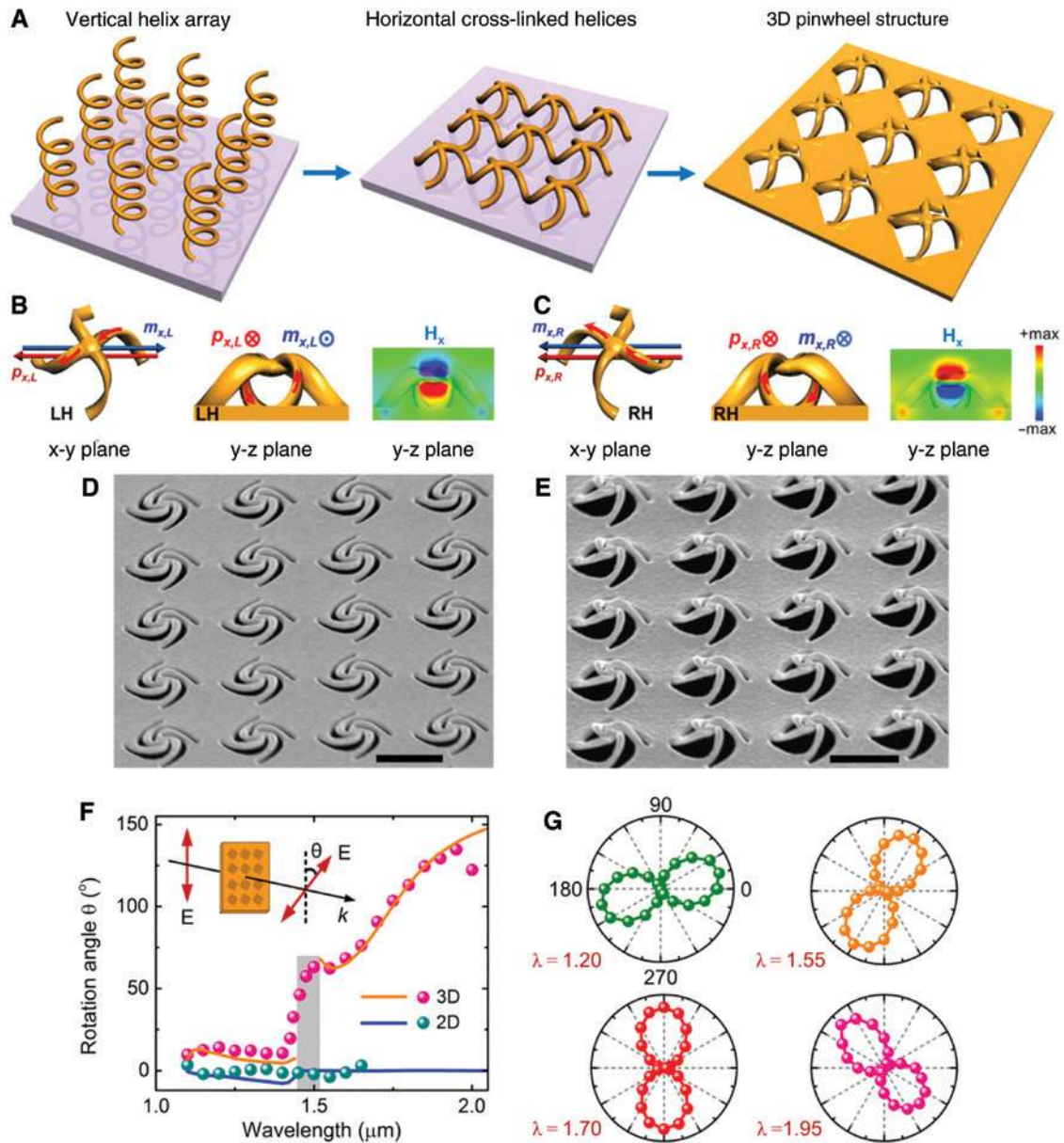
Figure 9: Giant 3D optical chirality enabled by close-loop nano-kirigami [39].
(A) Schematic of a vertical helix array, horizontal cross-linked helices, and a 3D pinwheel array, which show the evolution of the designed pinwheel structure. (B, C) Illustration of the responses to the electric field (E_x) of incident light for the left-handed (LH) and right-handed (RH) twisted pinwheels in (left) x–y plane and (middle) y–z plane, respectively. (right) Calculated magnetic field (H_x) at the wavelength 1.7 μm in the y–z plane ($x = 0$) under x-polarized excitation. The direction of H_x at center part of the pinwheels agrees well with the illustration. (D, E) SEM images of left-handed (LH) pinwheel arrays (D) before and (E) after global FIB irradiation, respectively. Scale bars: 1 μm. (F) Measured (circular points) and calculated (solid lines) linear polarization rotation angle (θ) versus wavelength for 3D and 2D LH pinwheels, respectively. (Inset) Schematic of the linear polarization rotation. (G) Polar plots of experimental transmission versus detection polarization angle at specific wavelengths as noted for the 3D LH pinwheels.

the shifting direction is opposite between the RCP and LCP spots. Since the structure is merely modulated along the x-axis (Figure 10B), this clear shift in the y-direction is actually perpendicular to the changing direction of the dielectric constant, which is similar to the intriguing photonic SHE [55], which arises from the spin−orbit interaction of light. The mechanism behind this is that the dramatic phase gradient in the x-direction breaks the axial symmetry of the interface and makes the diffracted light to propagate along a curved trajectory [40].
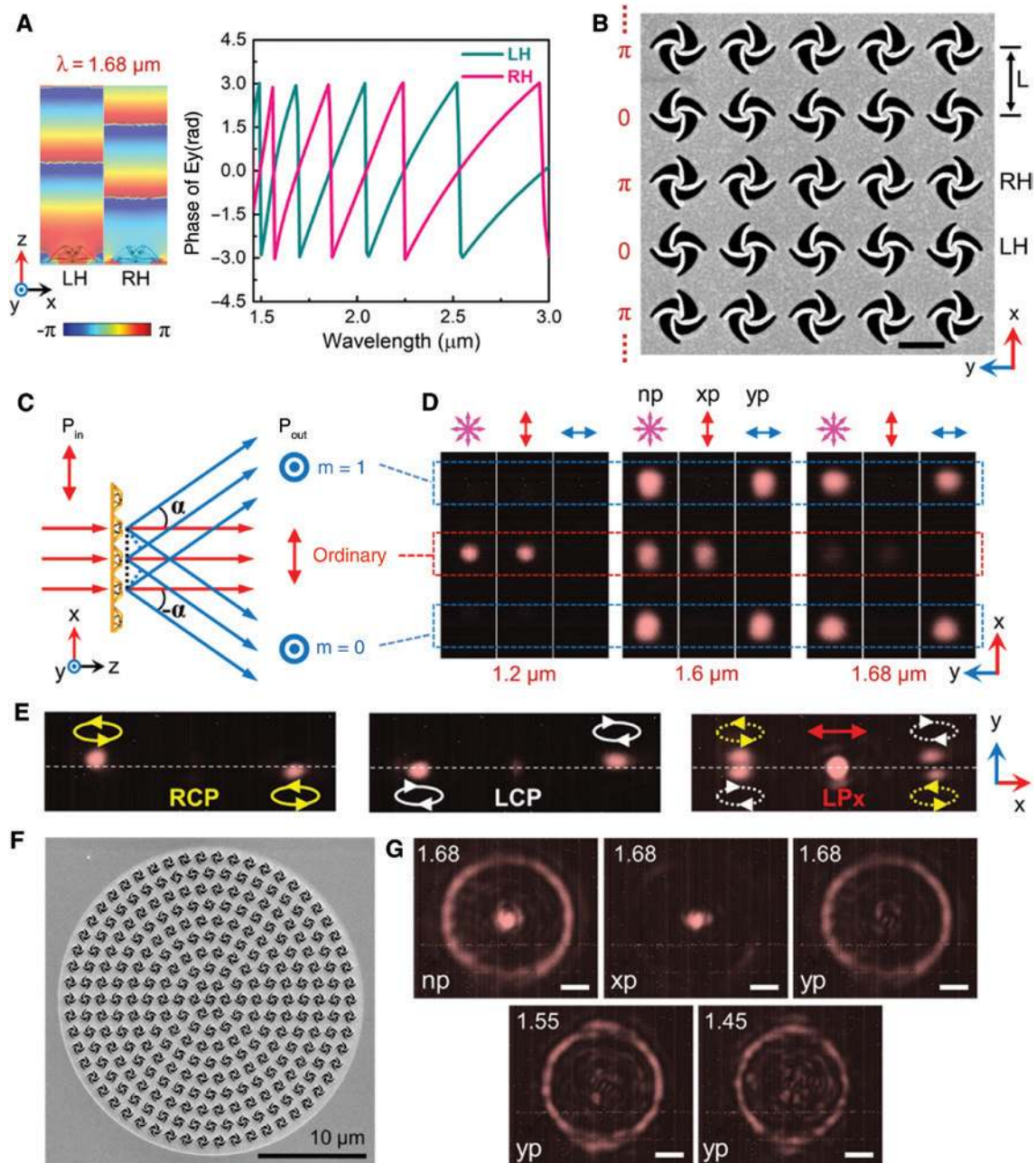
Figure 10: Phase and polarization manipulation [40].
(A) Phase diagram and phase spectra of the transmitted y-polarized electric-field (E_y) under x-polarized incidence, for pinwheels with LH and RH rotation, respectively. The phase differences between LH and RH remain constant around π for all wavelengths above the lattice period of 1.45 μm. (B) Top-view SEM image of a linear grating in which the LH and RH pinwheels are fabricated alternately along the x-direction. Under x-polarized incidence and for y-polarized transmission, there is a phase shift of π along the x-direction, as noted at the left side of the SEM image. Scale bars: 1 μm. (C) Schematic of the diffraction properties of the linear grating under x-polarized incidence. The converted y-polarized (cross-polarization) light is diffracted with angle $-\alpha$ and α for $m = 0$ and 1, respectively. (D) CCD camera images of the transmitted light spots at wavelengths 1.20, 1.60, and 1.68 μm, respectively, under detection with no polarization (np), x-polarization (xp), and y-polarization (yp). (E) CCD images of the spots of the diffracted (left) RCP and (middle) LCP beams under the illumination with LCP and RCP incident light, respectively. (right) CCD images of the beam spots with both incident and detection polarization aligned along the x-direction. Dashed circles indicate the positions of the equivalent RCP and LCP diffraction spots. The illumination power and imaging time were increased compared to other images. (F) Top-view SEM image of a circular grating with radial separation of 1.45 μm. (G) CCD camera images of transmitted light with np, xp, and yp detections under x-polarized incidence at wavelengths 1.68, 1.55, and 1.45 μm, respectively.

To satisfy momentum conservation, a geometric polarization rotation is introduced, which depends on the helicity of the incident light. As a result, the spin–orbit interaction changes the path of the circularly polarized light in the direction perpendicular to the phase gradient, which leads to the light spots with opposite handedness moving in opposite directions, as shown in Figure 10E.

With their robust polarization conversion and special phase properties, the LH and RH 3D pinwheels could be arranged in more flexible configurations, such as the radial grating shown in Figure 10F, which is insensitive to the polarization direction of the linearly polarized incident light [40]. Similar to that of linear grating, the center light spot in Figure 10G is from the transmission of the ordinary beams with the original polarization, while the outer rings are from the diffracted beams with cross-polarization. Moreover, it is found that the cross-polarized bright rings exist over broad band, as shown in Figure 10G, as expected, since the distribution of the phase difference is constant for wavelengths larger than 1.45 μm (Figure 10B). Such polarization and phase properties provide a robust strategy for the design of polarization-insensitive metasurfaces.

6 Conclusions and discussion

FIB-based tree-type and close-loop nano-kirigami can enable versatile 2D to 3D shape transformation and result in unique optical functions. Similar to macroscopic paper-cuts, the nano-kirigami utilizes high-dose FIB irradiation instead of knives/scissors to cut precise nanopatterns in the free-standing gold nanofilm and uses the same FIB with low-dose illumination instead of hands to fold/bend the 2D patterns into complex 3D shapes. It should be mentioned that, although the tree-type folding/bending methods have generated many exciting studies in the past decade, people have not recognized them as "nano-kirigami" approaches because of their relatively simple shape transformation compared to that in classical kirigami. In comparison, the FIB-based close-loop fabrication can be straightforwardly designated as a nano-kirigami method because the interlinked shape transformation occurs simultaneously across the whole sample region rather than localized at the sequentially folded areas. The topography-guided stress equilibrium among the subunits determines the final structural formation, which fits the traditional kirigami characteristics very well. It should be mentioned that the global irradiation with FIB is still a point-by-point scanning scheme but with a low irradiation dose swiftly repeated over the whole sample area. This can limit the performance of nano-kirigami with large patterns but can be overcome by irradiating the whole 2D structure simultaneously under other high-energy ion-based etching or implant systems in thin-film technologies. Our preliminary results show that this close-loop methodology can be applied to a wide variety of suspended thin-film materials and the fabrication systems are extendable to other ion-beam-based systems to achieve large-scale fabrications.

It is worthwhile to note that the characteristics of upward buckling, downward bending, complex rotation, and out-of-plane twisting in the close-loop nano-kirigami represent a new 3D nanofabrication scheme that is entirely different from conventional top-down, bottom-up, and self-assembly-based 3D nanofabrication techniques. More significantly, by developing accurate mechanical modeling during the complex nano-kirigami [39], an intriguing connection between nanomechanics and nanophotonics can be built, and it is feasible to inversely design exceptional 3D nanogeometries based on desired optical functionalities, providing a novel strategy for 3D intelligent nanofabrication.

Benefiting from the exceptional geometries with nano-kirigami, the exotic 3D nanostructures have produced versatile photonic functionalities, such as strongly interacting multiple Fano resonances, giant optical chirality, clear photonic SHE, and diffractive phase/polarization effects. More importantly, the suspended features endow the 3D nanostructures with potential characteristics such as reconfigurable nanophotonic and optomechanical devices by engineering the suspended subunits [56], like the scheme employed by commercial digital micromirror devices (DMD) in digital light processing (DLP) projection, and the related 3D printing industry. Therefore, the work here not only builds up a new nanofabrication concept and platform for diverse structural geometries and functionalities but also opens up new possibilities for the active configuration of versatile micro-/nanophotonic, electronic, and magnetic devices, for example, reconfigurable optical metamaterials and metasurfaces.

References

[1] https://en.wikipedia.org/wiki/Chinese_paper_cutting. Accessed August 8, 2018.

[2] https://baike.baidu.com/item/%E4%B8%AD%E5%9B%BD%E5%89%AA%E7%BA%B8/397259?fr=aladdin (in Chinese). Accessed August 8, 2018.

[3] https://www.origami-resource-center.com/history-of-origami.html. Accessed August 8, 2018.

[4] https://en.wikipedia.org/wiki/Kirigami. Accessed August 8, 2018.

[5] Zirbel SA, Lang RJ, Thomson MW, et al. Accommodating thickness in origami-based deployable arrays. J Mech Design 2013;135:111005.

[6] Rogers J, Huang YG, Schmidt OG, Gracias DH. Origami MEMS and NEMS. MRS Bull 2016;41:123–9.

[7] Deng JW, Ji HX, Yan CL, et al. Naturally rolled-up C/Si/C trilayer nanomembranes as stable anodes for lithium-ion batteries with remarkable cycling performance. Angew Chem Int Ed 2013;52:2326–30.

[8] Kuribayashi K, Tsuchiya K, You Z, et al. Self-deployable origami stent grafts as a biomedical application of Ni-rich TiNi shape memory alloy foil. Mater Sci Eng A Struct 2006;419:131–7.

[9] Silverberg JL, Evans AA, McLeod L, et al. Using origami design principles to fold reprogrammable mechanical metamaterials. Science 2014;345:647–50.

[10] Blees MK, Barnard AW, Rose PA, et al. Graphene kirigami. Nature 2015;524:204–7.

[11] Yasuda H, Chong C, Charalampidis EG, Kevrekidis PG, Yang J. Formation of refaction waves in origami-based metamaterials. Phys Rev E 2016;93:043004.

[12] Lamoureux A, Lee K, Shlian M, Forrest SR, Shtein M. Dynamic kirigami structures for integrated solar tracking. Nat Commun 2015;6:8092.

[13] Wang ZJ, Jing LQ, Yao K, et al. Origami-based reconfigurable metamaterials for tunable chirality. Adv Mater 2017;29:1700412.

[14] Momeni F, Hassani NSMM, Liu X, Ni J. A review of 4D printing. Mater Design 2017;122:42–79.

[15] Zhang YH, Zhang F, Yan Z, et al. Printing, folding and assembly methods for forming 3D mesostructures in advanced materials. Nat Rev Mater 2017;2:17019.

[16] Zhang YH, Yan Z, Nan KW, et al. A mechanically driven form of Kirigami as a route to 3D mesostructures in micro/nanomembranes. Proc Natl Acad Sci U S A 2015;112:11757–64.

[17] Cui JX, Adams JGM, Zhu Y. Pop-up assembly of 3D structures actuated by heat shrinkable polymers. Smart Mater Struct 2017;26:125011.

[18] Gansel JK, Thiel M, Rill MS, et al. Gold helix photonic metamaterial as broadband circular polarizer. Science 2009;325:1513–5.

[19] Turner MD, Saba M, Zhang QM, Cumming BP, Schroder-Turk GE, Gu M. Miniature chiral beamsplitter based on gyroid photonic crystals. Nat Photonics 2013;7:801–5.

[20] Liu N, Guo HC, Fu LW, Kaiser S, Schweizer H, Giessen H. Three-dimensional photonic metamaterials at optical frequencies. Nat Mater 2008;7:31–7.

[21] Chen Z, Huang GS, Trase I, Han XM, Mei YF. Mechanical self-assembly of a strain-engineered flexible layer: wrinkling, rolling, and twisting. Phys Rev Appl 2016;5:017001.

[22] Peraza-Hernandez EA, Hartl DJ, Malak RJ, Lagoudas DC. Origami-inspired active structures: a synthesis and review. Smart Mater Struct 2014;23:094001.

[23] Xu LZ, Shyu TC, Kotov NA. Origami and kirigami nanocomposites. ACS Nano 2017;11:7587–99.

[24] Melngailis J. Focused ion-beam technology and applications. J Vac Sci Technol B 1987;5:469–95.

[25] Utke I, Hoffmann P, Melngailis J. Gas-assisted focused electron beam and ion beam processing and fabrication. J Vac Sci Technol B 2008;26:1197–276.

[26] Xia L, Wu WG, Xu J, Hao YL, Wang YY. 3D nanohelix fabrication and 3D nanometer assembly by focused ion beam stress-introducing technique. Proc IEEE Micr Elect 2006;118–21.

[27] Arora WJ, Sijbrandij S, Stern L, Notte J, Smith HI, Barbastathis G. Membrane folding by helium ion implantation for three-dimensional device fabrication. J Vac Sci Technol B 2007;25:2184–7.

[28] Arora WJ, Smith HI, Barbastathis G. Membrane folding by ion implantation induced stress to fabricate three-dimensional nanostructures. Microelectron Eng 2007;84:1454–8.

[29] Chalapat K, Chekurov N, Li J, Paraoanu GS. Ion-beam assisted self-assembly of metallic nanostructures. Nucl Instrum Meth B 2012;272:202–5.

[30] Cui AJ, Liu Z, Li JF, et al. Directly patterned substrate-free plasmonic "nanograter" structures with unusual Fano resonances. Light Sci Appl 2015;4:e308.

[31] Liu ZG, Liu Z, Li JF, et al. 3D conductive coupling for efficient generation of prominent Fano resonances in metamaterials. Sci Rep UK 2016;6:27817.

[32] Chalapat K, Chekurov N, Jiang H, Li J, Parviz B, Paraoanu GS. Self-organized origami structures via ion-induced plastic strain. Adv Mater 2013;25:91–5.

[33] Mao YF, Pan YN, Zhang WH, Zhu R, Xu J, Wu WG. Multi-direction-tunable three-dimensional meta-atoms for reversible switching between midwave and long-wave infrared regimes. Nano Lett 2016;16:7025–9.

[34] Liu Z, Du S, Cui AJ, et al. High-quality-factor mid-infrared toroidal excitation in folded 3D metamaterials. Adv Mater 2017;29:1606298.

[35] Samayoa MJ, Haque MA, Cohen PH. Focused ion beam irradiation effects on nanoscale freestanding thin films. J Micromech Microeng 2008;18:095005.

[36] Rajput NS, Banerjee A, Verma HC. Electron- and ion-beam-induced maneuvering of nanostructures: phenomenon and applications. Nanotechnology 2011;22:485302.

[37] Liu ZG, Li JF, Liu Z, et al. Fano resonance Rabi splitting of surface plasmons. Sci Rep UK 2017;7:8010.

[38] Mao YF, Zheng Y, Li C, et al. Programmable bidirectional folding of metallic thin films for 3D chiral optical antennas. Adv Mater 2017;29:1606482.

[39] Liu ZG, Du HF, Li JF, Lu L, Li Z-Y, Fang NX, Nano-kirigami with giant optical chirality. Sci Adv 2018;4:eaat4436.

[40] Liu ZG, Du HF, Li Z-Y, Fang NX, Li JF. Nano-kirigami metasurfaces by focused-ion-beam induced close-loop transformation. APL Photonics 2018;3:100803.

[41] Antonio T, Claudio M. Modelling and control of mechanisms and robots. Singapore, World Scientific Publishing Company, 1996.

[42] Buchner T. Kinematics of 3D folding structures for nano-structured origami (TM). Diplomarbeit thesis, Massachusetts Institute of Technology, 2003.

[43] Tian XM, Liu ZG, Lin H, Jia BH, Li Z-Y, Li JF. Five-fold plasmonic Fano resonances with giant bisignate circular dichroism. Nanoscale 2018;10:16630–7.

[44] Fano U. Effects of configuration interaction on intensities and phase shifts. Phys Rev 1961;124:1866–78.

[45] Zhao R, Zhang L, Zhou J, Koschny T, Soukoulis CM. Conjugated gammadion chiral metamaterial with uniaxial optical activity and negative refractive index. Phys Rev B 2011;83:035105.

[46] Wang ZJ, Cheng F, Winsor T, Liu YM. Optical chiral metamaterials: a review of the fundamentals, fabrication methods and applications. Nanotechnology 2016;27:412001.

[47] Rodrigues SP, Lan SF, Kang L, et al. Intensity-dependent modulation of optically active signals in a chiral metamaterial. Nat Commun 2017;8:14602.

[48] Hentschel M, Schaferling M, Duan XY, Giessen H, Liu N. Chiral plasmonics. Sci Adv 2017;3:1602735.

[49] Zhu AY, Chen CWT, Aun Z, et al. Giant intrinsic chiro-optical activity in planar dielectric nanostructures. Light Sci Appl 2018;7:e17158.

[50] Yu N, Genevet P, Kats MA, et al. Light propagation with phase discontinuities: generalized laws of reflection and refraction. Science 2011;334:333–7.

[51] Zhang L, Mei ST, Huang K, Qiu CW. Advances in full control of electromagnetic waves with metasurfaces. Adv Opt Mater 2016;4:818–33.

[52] Hsiao HH, Chu CH, Tsai DP. Fundamentals and applications of metasurfaces. Small Methods 2017;1:1600064.

[53] Genevet P, Capasso F, Aieta F, Khorasaninejad M, Devlin R. Recent advances in planar optics: from plasmonic to dielectric metasurfaces. Optica 2017;4:139–52.

[54] Chen HT, Taylor AJ, Yu NF. A review of metasurfaces: physics and applications. Rep Prog Phys 2016;79:076401.

[55] Ling XH, Zhou XX, Huang K, et al. Recent advances in the spin Hall effect of light. Rep Progress Phys 2017;80:066401.

[56] Ong JR, Chu HS, Chen VHJ, Zhu AYT, Genevet P. Freestanding dielectric nanohole array metasurface for mid-infrared wavelength applications. Opt Lett 2017;42:2639–42.